

Article

Meso-Scale Formulation of a Cracked-Hinge Model for Hybrid Fiber-Reinforced Cement Composites

Enzo Martinelli ^{1,2,*} , Marco Pepe ^{1,2}  and Fernando Fraternali ¹ 

¹ Department of Civil Engineering, University of Salerno, 84084 Fisciano, Italy; mapepe@unisa.it (M.P.); f.fraternali@unisa.it (F.F.)

² TESIS srl, 84084 Fisciano, Italy

* Correspondence: e.martinelli@unisa.it; Tel.: +39-081-96-4098

Received: 28 July 2020; Accepted: 27 August 2020; Published: 1 September 2020



Abstract: This study presents a non-linear cracked-hinge model for the post-cracking response of fiber-reinforced cementitious composites loaded in bending. The proposed displacement-based model follows a meso-mechanical approach, which makes it possible to consider explicitly the random distribution and orientation of the reinforcing fibers. Moreover, the model allows for considering two different fiber typologies whereas the cement matrix is modelled as a homogeneous material. The proposed mechanical model combines a fracture-based, stress-crack opening relationship for the cementitious matrix with generalized laws aimed to capture the crack-bridging effect played by the reinforcing fibers. These laws are derived by considering both the fiber-to-matrix bond mechanism and fiber anchoring action possibly due to hooked ends. The paper includes a numerical implementation of the proposed theory, which is validated against experimental results dealing with fiber-reinforced cement composites reinforced with different short fibers. The excellent theory vs. experiment matching demonstrates the high technical potential of the presented model, obtained at a reasonable computational cost.

Keywords: fiber-reinforced cementitious composites; cracked-hinge model; meso-scale model; numerical model; hybrid FRCC

1. Introduction

Fiber-reinforced cementitious composites (FRCCs) are a class of concrete-like material developed in the last two decades with the aim of mitigating the inherent fragility of concrete in tension [1]. Several types of fiber are currently adopted as spread reinforcement in FRCCs, which range from the very common steel fibers [2–5], to the ones either made of plastics [6] or, more recently, obtained from plants [7,8], or produced by recycling waste tires [9–11]. Moreover, FRCCs can also be produced by blending different types of fibers to produce a class of composites often referred to as hybrid-FRCCs (Hy-FRCCs) with the aim to mobilize a synergistic action from each fiber [12–17].

Plenty of experimental results are available in the literature, which demonstrate the capability of fibers to bridge cracks developing throughout a cement-based matrix and, hence, enhancing their post-cracking performance in compression [18], but especially in tension [19] and bending [20,21].

Quantitative measures and indices have been defined in well-established codes and guidelines [22–27] with the aim of characterizing the post-cracking response of FRCCs, especially in specimens subjected to either three- or four-point bending. Specifically, these toughness indices are determined on the experimentally obtained force-displacement curve, generally focusing on either the crack-mouth-opening-displacement (CMOD) or the crack-tip-opening-displacement (CTOD).

However, no theoretical model has proven capable so far of being able to predict these force-CMOD/CTOD curves, based solely on the properties of the matrix mixture and the type and amount of fibers.

Some theoretical models are available in the literature and these often follow the Smeared Crack approach, such as the flow theory of plasticity [28], continuum damage theories [29] and microplane formulations [30]. However, other models are based on the discrete crack approach and assume discontinuous displacement fields as part of either X-FEM procedures [31], interface elements [32], or lattice and particle approaches [33].

This paper proposes a meso-scale based model intended at taking into account explicitly the behavior of the two typical “phases” of FRCCs, namely the cement-based matrix and the spread fiber reinforcement phases, along with their interaction. The model kinematics is inspired to the so-called “cracked-hinge” approach [34,35], but the crack-bridging effect of fibers is explicitly simulated and the presence of two different fiber types is also considered. Moreover, the proposed model aims at reproducing explicitly the random spatial distribution and orientation of fibers inside the FRCC matrix. In this sense, the proposed model can be intended as an extension of the one proposed by [36], where the number of fibers (of the same type, mainly made of steel) crossing the opening crack was based on statistical considerations. Therefore, the proposed meso-mechanical model aims at predicting the post-cracking behavior of FRCCs subjected to bending, starting with the formulation of appropriate mechanical models of the matrix, fibers, and their interface.

2. Formulation of a Meso-Mechanical Cracked-Hinge Model

2.1. Geometric Definition and Main Kinematic Assumptions

The cement-based beam is schematized as a prism of length L , width b , and depth h . Then, a Cartesian reference system is set at the centroid of the gross section at mid-span of the beam. In addition, a transverse “notch” (whose depth is denoted with δ) is present at the midspan section (Figure 1).

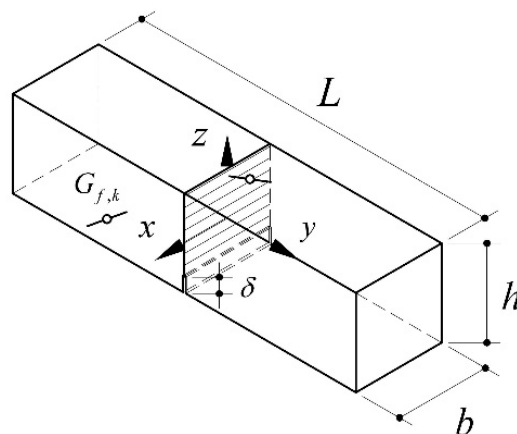


Figure 1. Geometric scheme and definitions of the concrete beam.

Since the model aims at considering explicitly the contribution of the fiber-bridging effect across the two edges of cracks opening within the cementitious matrix, the model firstly generates the distribution of such fibers within the beam region. Specifically, as the total geometric ratio of fibers is defined ρ_f , along with both their diameter d_f and length l_f , the total number of fibers n_f can be easily determined:

$$n_f = \frac{V_f}{V_{fi}} = \frac{\rho_f \cdot V_c}{V_{fi}} = \frac{\rho_f (L \cdot b \cdot h)}{\left(\pi \cdot \frac{d_f^2}{4} \cdot l_f\right)} \quad (1)$$

where V_f is the volume of the fibers, V_{fi} is the volume of the single fiber, and V_c is the volume of the cement-based matrix.

It is worth highlighting that, if two different types of fibers are actually present within the matrix, their numbers $n_{f,1}$ and $n_{f,2}$ can be easily determined by means of Equation (1) considering the densities $\rho_{f,1}$ and $\rho_{f,2}$ of the materials they are made out of. However, for the sake of simplicity (and with no conceptual limitation) the formulation proposed hereafter is based on a single type of fibers.

Then, based on a random distribution within the prismatic beam volume, both the three centroidal coordinates $x_{f,k}$, $y_{f,k}$ and $z_{f,k}$ (with k ranging between 1 and n_f) and the two relevant angles $\alpha_{x,k}$ and $\alpha_{z,k}$ (Figure 2) can be randomly generated as follows:

$$x_{f,k} = b \cdot \text{rnd}_{(-0.5;+0.5)} \tag{2}$$

$$y_{f,k} = L \cdot \text{rnd}_{(-0.5;+0.5)} \tag{3}$$

$$z_{f,k} = h \cdot \text{rnd}_{(-0.5;+0.5)} \tag{4}$$

$$\alpha_{x,k} = \pi/2 \cdot \text{rnd}_{(-0.5;+0.5)} \tag{5}$$

$$\alpha_{z,k} = \pi/2 \cdot \text{rnd}_{(-0.5;+0.5)} \tag{6}$$

where $\text{rnd}_{(-0.5;+0.5)}$ is a randomly generated real numbers included between -0.5 and 0.5 . The coordinates of the two ends of the k -th fiber can be easily determined and the fiber position can be accepted if both ends are included within the beam prism.

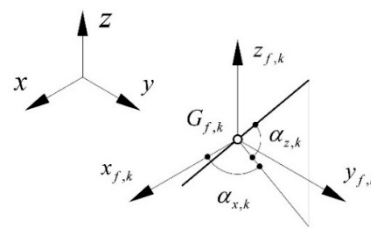


Figure 2. Geometric parameters defining the position of the generic fiber within the concrete beam.

Although the various types of fibers considered in the FRCCs could not present constant geometrical characteristics, this formulation is restricted to assuming, for each type of fiber, invariant geometrical properties, such as diameter d_f (and, consequently section area A_f), as well as length l_f .

In a cracked-hinge model, it is accepted that flexibility is distributed in a portion s of the span length of the beam, while the remaining part is supposed to respond as a rigid body (Figure 3).

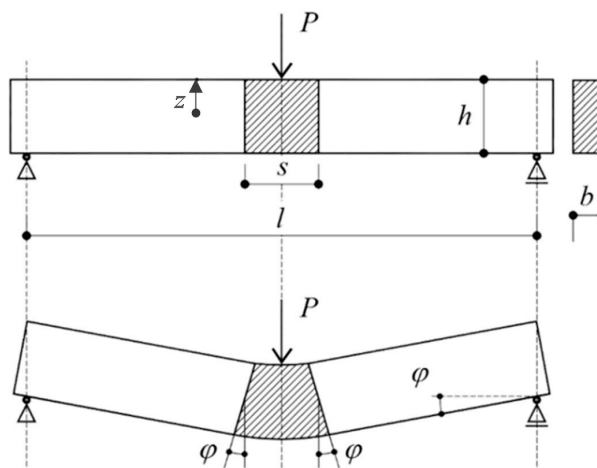


Figure 3. Kinematics of the Cracked-Hinge Model.

The flexible part is modeled as an array of n_c independent elastic springs or “strips” aligned with the longitudinal axis of the member (“strip model”) [34–36]. Whose force-displacement response is obtained by considering a “strip model” of the hinged region (Figure 4), and generalized constitutive relationships describing the stress release across the forming cracks and the extraction of fibers that bridge them.

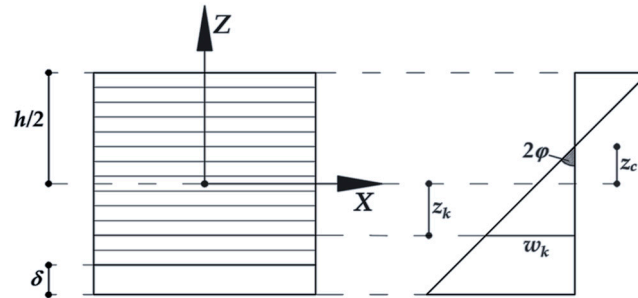


Figure 4. Strip discretization of the notched cross section and resulting distribution of axial strains/displacements.

A simple kinematics can be established for the beam, if it is assumed that rotations of the two rigid blocks take place around the neutral axis of the cracked-hinge section, whose position is described by z_c (Figure 4).

Based on this assumption, the rotation φ (Figure 3) can be taken as the main generalized displacement parameters, whereas the beam deflection at midspan v , the crack-tip opening displacement (CTOD), and the crack-mouth opening displacement (CMOD) can be determined as follows:

$$v = \varphi \cdot L/2 \tag{7}$$

$$CMOD = \varphi \cdot (h/2 + z_c) \tag{8}$$

$$CTOD = \varphi \cdot (h/2 + z_c - \delta) \tag{9}$$

2.2. Equilibrium Equations

Equations (7)–(9) show that the position of the neutral axis (z_c) plays a fundamental role in determining the relevant displacement components of the beam response in bending. For each value of the imposed rotation φ , the end points of a generic segment forming the “process zone” s (Figure 3) undergo the following relative axial displacement:

$$w(z) = 2\varphi \cdot (z_c - z) \tag{10}$$

where z denotes the transverse coordinate of the strip (Figure 4).

Based on this observation, the present model assumes the following expressions of the axial displacement w_k and the axial strain ε_k exhibited by the k -th strip ($k = 1, \dots, n_c$):

$$w_k = 2\varphi \cdot (z_c - z_k) \tag{11}$$

$$\varepsilon_k = \frac{2\varphi \cdot (z_c - z_k)}{s} \tag{12}$$

The average axial stress $\sigma_{c,k}$ across the k -th strip can be determined either as a function of the axial strain ε_k defined of Equation (12) (before cracking) or depending on the crack-opening displacements

w_k in Equation (11) (after cracking). Therefore, it depends on the position of the strip centroid z_k and can be expressed as a function of both the neutral axis position z_c and the imposed rotation φ as follows:

$$\sigma_{c,k} = \sigma_c(z_k; z_c, \varphi) \tag{13}$$

Details about the constitutive laws specifically adopted for the matrix in this study are described in Section 3.2.

As for the contribution of fibers, it is controlled by the crack opening displacement w_k expressed in Equation (11). Moreover, the present formulation assumes a complete reorientation of fibers crossing the cracked section: regardless of their initial inclination (described by the angles $\alpha_{x,k}$ and $\alpha_{z,k}$) they are supposed to exert axial stresses $\sigma_{f,k}$ depending on both the lateral bond stress τ mobilized throughout the lateral area and the possible contribution F of the hooked end (see Section 3.3). Therefore, since both contributions depend on w_k , the axial stress $\sigma_{f,k}$ mobilized in the k -th fiber crossing the midspan section can be formally expressed as follows:

$$\sigma_{f,k} = \sigma_f(z_{f,k}; z_c, \varphi) \tag{14}$$

Therefore, the following equilibrium equation can be written for each imposed rotation angle φ :

$$b \cdot \Delta z \cdot \sum_{k=1}^{n_c} \sigma_{c,k}(z_k; z_c, \varphi) + A_f \cdot \sum_{k=1}^{n'_f} \sigma_{f,k}(z_k; z_c, \varphi) = 0 \tag{15}$$

and, hence, the position of the neutral axis can be determined. Therefore, the bending moment corresponding to the imposed rotation φ can be easily evaluated as follows:

$$M(\varphi) = b \cdot \Delta z \cdot \sum_{k=1}^{n_c} \sigma_{c,k}(z_k; \bar{z}_c, \varphi) \cdot z_k + A_f \cdot \sum_{k=1}^{n'_f} \sigma_{f,k}(z_k; \bar{z}_c, \varphi) \cdot z_k \tag{16}$$

3. Numerical Implementation

3.1. Geometry of the FRCC Beam

First of all, it is necessary to define some preliminary information, i.e., the geometry of the beam, in terms of L (length of the specimen assessed as the distance between the lower supports of the test machine), b and h (width and height of the specimen, respectively).

For the definition of the beam length, it is necessary to set the type of loading scheme, which can either be on three-points ($L = 500$ mm in accordance with the [22–24]) or four-points ($L = 450$ mm in accordance with the [25,26]). Then, the moment distribution can be easily determined.

Once the geometric characteristics of the beam have been defined, the discretization of the hinge formation zone is defined in a certain number of layers.

3.2. Stress-Strain and Stress-Crack Opening for Cementitious Matrix

According to the fictitious crack approach, a linear elastic behavior is assumed when the section is uncracked, while after the formation of the crack, a softening constitutive law is accepted where bridging stresses across the crack are defined in terms of the crack width.

For uncracked concrete, in accordance with [27], a bilinear stress–strain relation may be used, as given in the following equations:

$$\sigma_{ct} = \begin{cases} (a) \Rightarrow E_{ct} \cdot \varepsilon_{ct} & \text{for } \varepsilon_{ct} \leq 0.9 \frac{f_{ctm}}{E_{ct}} \\ (b) \Rightarrow f_{ctm} \cdot \left(1 - 0.1 \cdot \frac{0.00015 - \varepsilon_{ct}}{0.00015 - 0.9 \cdot \frac{f_{ctm}}{E_{ct}}} \right) & \text{for } 0.9 \frac{f_{ctm}}{E_{ct}} \leq \varepsilon_{ct} \leq 0.00015 \end{cases} \tag{17}$$

where:

- E_{ct} is the tangent modulus of elasticity (expressed in MPa) in tension;
- ε_{ct} is the tensile strain,
- σ_{ct} is the tensile stress (expressed in MPa);
- f_{ctm} is the tensile strength (expressed in MPa).

The E_{ct} and f_{ctm} can be evaluated as follow [27]:

$$E_{ct} = \frac{E_c}{2} = \frac{22000 \cdot \left(\frac{f_{cm}}{10}\right)^{0.3}}{2} \tag{18}$$

$$f_{ctm} = 0.3 \cdot (f_{cm} - 8)^{2/3} \tag{19}$$

where E_c and f_{cm} represent the elastic modulus and the mean cylindrical strength in compression, respectively [27].

The bilinear stress-strain relationship in Equation (17) describes the contribution of the matrix in tension before cracking. As the tensile strain ε_k of the generic matrix strip achieves the conventional value 0.00015 assumed as upper limit in in Equation (17b), a crack is supposed to open in that strip and, then, the residual stress $\sigma_{c,t}$ has to be expressed as function of the crack opening w represented in Figure 5 [27]:

$$\sigma_{ct} = \begin{cases} f_{ctm} \cdot \left(1.0 - 0.8 \cdot \frac{w}{w_1}\right) \text{ for } w \leq w_1 \\ f_{ctm} \cdot \left(0.25 - 0.05 \cdot \frac{w}{w_1}\right) \text{ for } w_1 \leq w \leq w_c \end{cases} \tag{20}$$

with:

$$w_1 = \frac{G_F}{f_{ct}} \tag{21}$$

$$w_c = 5 \cdot w_1 \tag{22}$$

where G_F is the fracture energy which can be estimated as follow:

$$G_F = G_{F0} \cdot \left(\frac{f_{cm}}{f_{cm0}}\right)^{0.18} \tag{23}$$

with G_{F0} and f_{cm0} equal to 0.11 N/mm and 10 MPa, respectively [27].

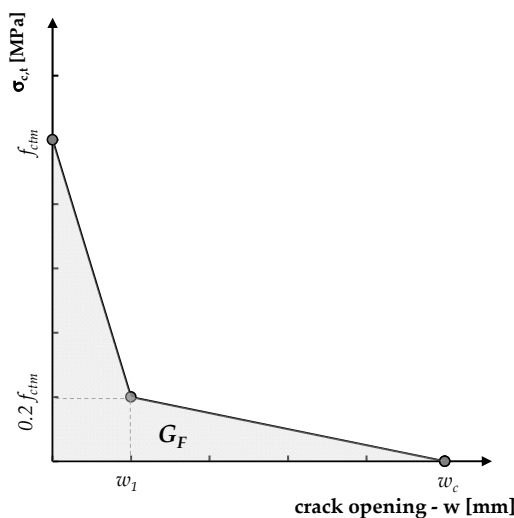


Figure 5. Stress-crack opening relationship for cracked concrete.

3.3. Bond of Spread Fiber Reinforcement Embedded within the Cementitious Matrix

As for fibers, their response is supposed to result from the rigid body slipping of one of the two parts (actually, the shortest one) embedded in the two sides of the crack. Despite this, in the model proposed herein, it is assumed that the generic fiber intercepts the plane of formation of the crack exactly in the middle of its length, so that the unthreading conditions, on the right and left of the crack, are symmetrical. For the bond of the fibers, the two following contributions are considered (Figure 6):

- the distributed bond throughout the lateral surface of the fiber, which is modelled through a bilinear bond-slip law (Figure 6a) which is defined by the three parameters τ_{max} , s_{el} and s_u and is governed by the fiber fracture energy ($G_{F,fiber}$);
- the concentrated force at the end hook (if present), which is described by a trilinear force-slip law (Figure 6b) defined by the maximum force F_{sp} attained at the slip $s_{e,sp}$, the residual force $F_{sp,r}$ attained at a displacement $s_{r,sp}$ and sustained up to an ultimate slip value $s_{u,sp}$.

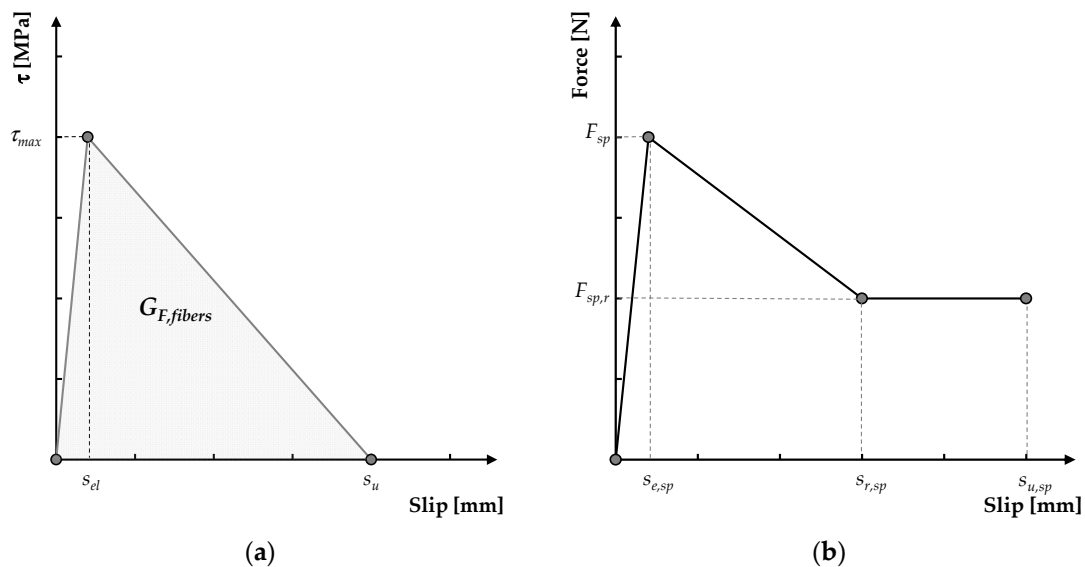


Figure 6. Bond-slip law for short fibers embedded within the cementitious matrix: (a) longitudinal tangential stresses during slipping and (b) simulation of the hooked end.

3.4. Force vs. Crack Opening Curves and Ductility Indices

Once the input parameters have been defined, it is possible to run the analysis by setting the number of simulations to be performed. Taking the input data above defined, the numerical procedure generates and positions the short fibers (Equations (1)–(6)). Subsequently, it assesses the stress reached in the cement-based matrix (by Equation (13)) as well as the contribution given by the fibers (by Equation (14)) in terms of strength. In this way, it is possible to define the position of the neutral axis (by Equation (15)) and, consequently, by integrating the axial tensions that arise on the cross section, the bending moment, through Equation (16). Finally, the load–displacement trend, expressed in terms of *CMOD* or *CTOD*, is simulated through the Equations (8) and (9).

The next step is the evaluation of the characteristic parameters defining the post-cracking response of the FRCCs. This is performed by introducing some ductility indices, by means of which it is possible to trace the numerical value of the areas underlying the load-*CTOD* curve, expression of the absorbed energy, and consequently, of the equivalent resistances and ductility indices.

More specifically, this evaluation is carried out as described by the UNI 11039/2003 [25,26] by introducing the following parameters: first crack strength (f_{1f}), work capacity indices (U_1 and U_2), the equivalent post-cracking strengths and ductility indices (D_0 and D_1)

The first crack strength (f_{1f}) is defined as follow:

$$f_{1f} = \frac{P_{1f} \cdot l}{h \cdot (b - \delta)^2} \quad (24)$$

where P_{1f} represents the first crack load (in N).

The work capacity indices (U_1 and U_2) represent the areas under the vertical load P - $CTOD$ curve in a representative range for the Serviceability Limit State (i.e., considering a $CTOD$ ranging between $CTOD_0$ and $CTOD_0 + 0.6$ mm) and for the Ultimate State (i.e., considering $CTOD$ ranges between $CTOD_0 + 0.6$ mm and $CTOD_0 + 3.0$ mm), respectively.

$$U_1 = \int_{0.00}^{0.60} P(CTOD) d(CTOD) \quad (25)$$

$$U_2 = \int_{0.60}^{3.00} P(CTOD) d(CTOD) \quad (26)$$

Regarding the two “equivalent post-cracking strengths” ($f_{eq(0-0.6)}$ and $f_{eq(0.6-3)}$), the first is supposed to be relevant for the serviceability limit state (evaluated as a function of the U_1 parameter), whereas the second one is relevant for the ultimate state (evaluated as a function of the U_2 parameter).

Finally, the “ductility indices” (D_0 and D_1) can be determined with the following equations:

$$D_0 = \frac{f_{eq(0-0.6)}}{f_{1f}}, \quad (27)$$

$$D_1 = \frac{f_{eq(0.6-3)}}{f_{eq(0-0.6)}}. \quad (28)$$

4. Model Validation

This section proposes a validation of the model based on experimental results already available in the literature, either in terms of applied force vs. crack-opening displacements ($CMOD$ or $CTOD$) or ductility indices [25,26]. Specifically, the experimental data considered for this purpose refer to FRC mixtures incorporating several types of short fibers [37,38]:

- industrial steel fibers (ISF);
- recycled steel fibers (RSF);
- polypropylene fibers (PPF).

Table 1 reports the relevant geometric and mechanical properties of the fibers. A uniform statistical distribution has been adopted for generating position and orientation of fibers according to Equations (2)–(6).

Table 1. Geometrical and mechanical properties of the short fibers.

Fiber Type	d_f (mm)	l_f (mm)	Hooked End	Tensile Strength (MPa)	Elastic Modulus (GPa)
ISF	0.550	33	Yes	>1200	210
RSF	0.255	26	Yes	>1200	210
PPF	0.032	12	No	400–500	3.5–3.9

In the two referenced experimental studies, several fiber-reinforced mixtures were produced by keeping unchanged the overall amount of fibers (i.e., 0.75% in volume) and considering several combinations as well as hybrid (i.e., including two type of fibers) systems (see Table 2).

Table 2. Fiber Reinforced Concrete mixtures [37,38].

Mixture	ISF (kg/m ³)	RSF (kg/m ³)	PPF (kg/m ³)	ISF (%)	RSF (%)	PPF (%)
ISF-FRC	60.0	-	-	0.750	-	-
RSF-FRC	-	60.0	-	-	0.750	-
PPF-FRC	-	-	6.8	-	-	0.750
Hybrid ISF-RSF FRC	30.0	30.0	30.0	0.375	0.375	-
Hybrid ISF-PPF FRC	45.0	-	1.7	0.550	-	0.200

The cementitious matrices of the above-mentioned mixtures were produced with Portland cement type II, a water-to-cement ratio equal to 0.50 and presented an average value of 20 MPa in terms of average cylindrical compressive strength [37,38]. The numerical simulations were run after calibrating the bond-slip laws between the fibers and the surrounding matrix (Figure 6). A summary of the calibrated values is reported in Table 3. It is worth highlighting that those values were obtained for each single type of fibers and utilized in the analyses also in the case of hybrid FRCC made by blending two different types of fibers. Based on a sensitivity analysis (whose results are omitted herein for the sake of brevity), $n_c = 20$ was assumed in Equations (15) and (16) and s was set to 300 mm.

Table 3. Calibrated values for the fibers bond-slip laws.

Parameter	ISF	RSF	PPF
τ_{max} (MPa)	3.8	2.8	0.9
s_{el} (mm)	0.125	0.130	0.04
s_u (mm)	20.0	20.0	8.0
F_{sp} (N)	160	36	-
$F_{sp,r}$ (N)	140	30	-
$s_{e,sp}$ (mm)	6.0	6.0	-
$s_{e,sp}$ (mm)	15.0	13.0	-
$s_{u,sp}$ (mm)	25.0	20.0	-

Figure 7 shows some representative comparisons between experimental and numerical curves. The black lines represent the average experimental curve and the gray area its scatter. On the other hand, the red curves represent the curves obtained by the numeral simulations (10 simulations for each case): the scatter of the numerical curves is due to the fact that, for each simulation, a random distribution of the fibers is generated and, consequently, the number of fibers crossing the cracked section is variable.

The curves reported in Figure 7 demonstrate that the numerical simulations are able to reproduce the experimental results in a satisfactory manner. This evidence is clearer when ISF and/or PPF fibers are employed, while some scatter is registered for the Hybrid ISF-RSF FRC mixtures. This can be attributed to the fact that the ISF and PPF are industrial products meanwhile the RSF are derived by processing the waste of end-of-life tires. For these reasons, the RSF fibers (being a recycled product) present variable geometric characteristic but, in the present model only the average values (in terms of fibers' diameter and length) are considered.

A more comprehensive comparison between the experimental and numerical analysis is performed in terms of work capacity and ductility indices (Figure 8). The points plotted in Figure 8 represent the average values of 1000 performed simulations for each type of mixture.

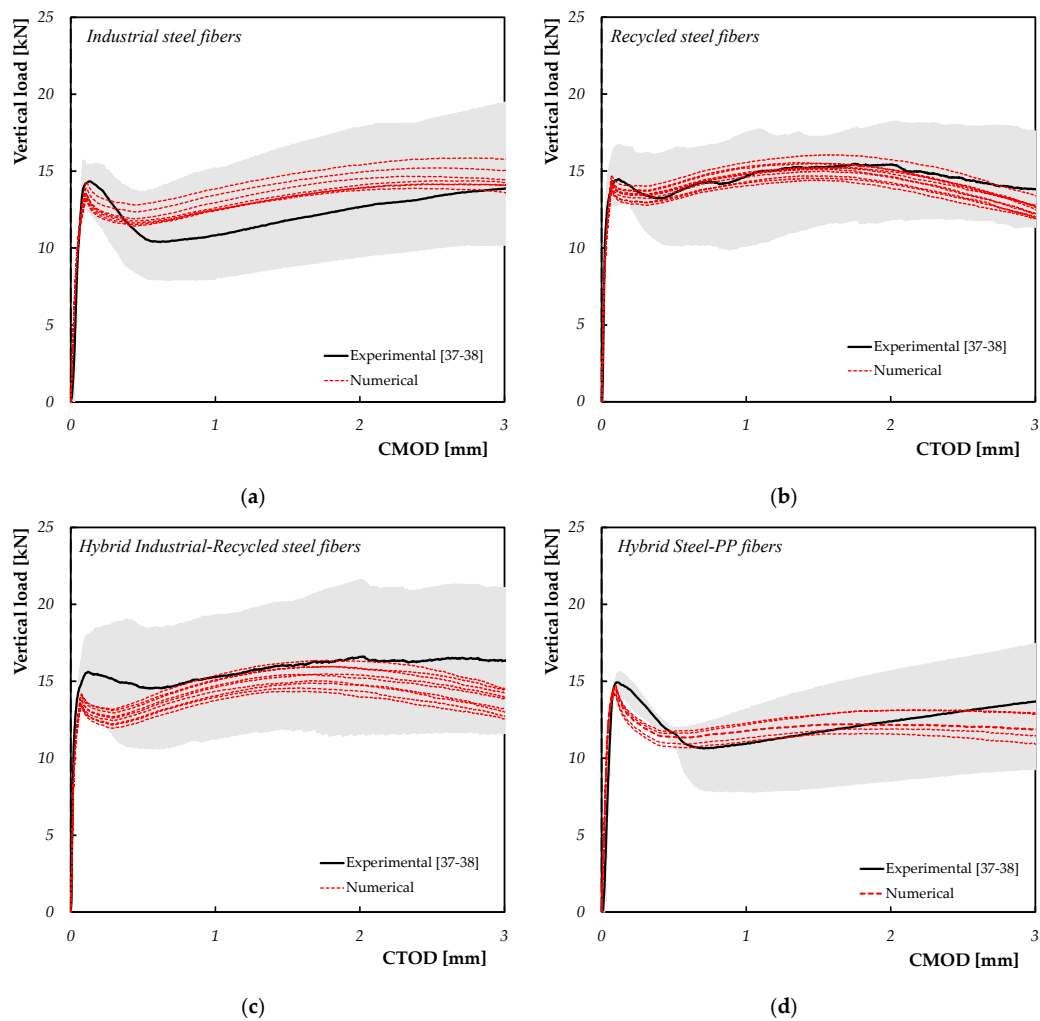


Figure 7. Representative numerical versus experimental data for (a) ISF-FRC, (b) RSF-FRC, (c) Hybrid ISF-RSF FRC and (d) Hybrid ISF-PPF FRC mixtures.

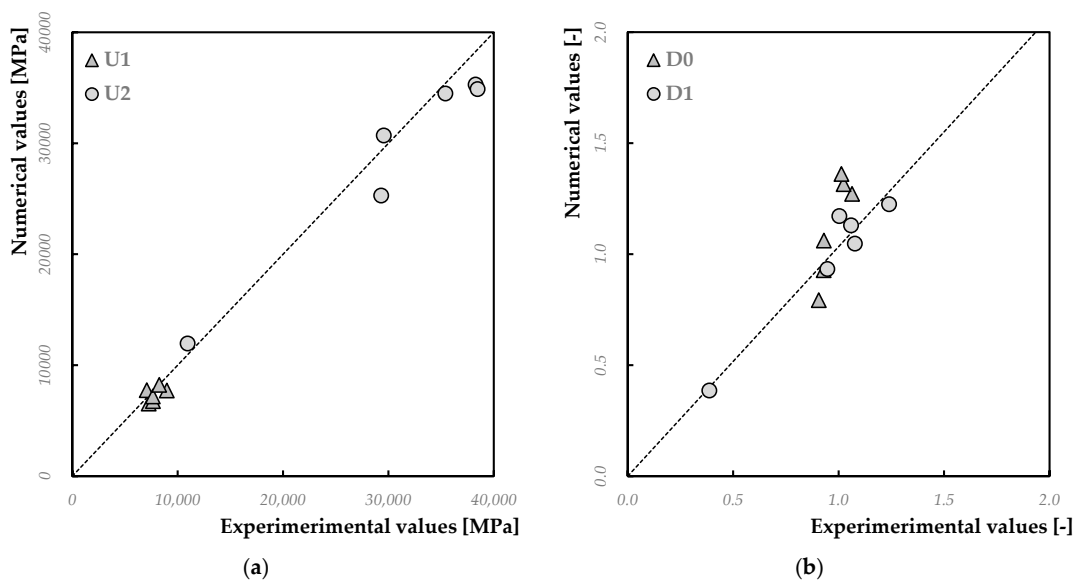


Figure 8. Numerical versus experimental data for (a) work capacity indices and (b) ductility indices.

In terms of work capacity indices (U_1 and U_2), it is possible to note (Figure 8a) how the model is able to simulate the behavior obtained from the experimental tests. As a matter of the fact, the RSF-FRC mixtures present results almost coincident both in terms of U_1 (8.23 Nm for the numerical model versus 8.25 Nm obtained in the experimental tests) and of U_2 (34.49 Nm in the numerical analysis and 35.40 Nm in the case of experimental data). Similar results are also obtained in the other cases, especially for the ISF-FRC mixtures.

On the other hand, as a general trend the numerical simulations tend to overestimate (of around 20–25%) the D_0 experimental values (Figure 8a). This difference is attributable to the underestimation of the first crack resistance f_{1f} (see for example Figure 7c), as D_0 is strictly related to the latter. Conversely, the simulated ductility index D_1 are closer to the corresponding experimental results (Figure 8b) and the scatter is often lower than 1–2%.

5. Conclusions

This paper presented a numerical model aimed at simulating the post-cracking response of FRCCs notched beams subjected to flexural loads. The cracked-hinge meso-mechanical model presented herein was also validated by comparing the results of experimental data already available in the literature. The following conclusions can be noted:

- The obtained results show that the cracked-hinge model is able to represent quite faithfully the post-cracking behavior of the fiber-reinforced composites. Particularly, it has been shown that the load-COD curves (both in terms of $CTOD$ and $CMOD$) are actually very close to the average experimental trend, especially for the mixtures reinforced with only industrial steel fibers.
- For the hybrid mixtures, however, the results are certainly more than satisfactory, but could be further improved by further developing the model with the aim to take into account explicitly of the individual variation of geometric properties for recycled fibers.
- The capability of the model to simulate the post-cracking behavior is clearly demonstrated. Further, the model is capable to reproduce the contribution of different types of fibers (either straight or hooked, made of steel or propylene) and this is a specific advantage of the proposed meso-mechanical approach;
- The agreement obtained in terms of load- $CMOD/CTOD$ curves is then reflected also in the characteristic parameters of the post-cracking behavior of the material. In fact, the values found are close to the experimental values in terms of work capacity and ductility indices.

Further evolutions of the present model are currently under development with the aim to generalise the theory presented in this study to fibers characterized by more complex features, such as embossments, curved profiles, or fractal geometries [39]. Such fibers may be 3D-printed in polymeric and metallic materials, so as to generate optimized fiber geometries and matrix–fiber fractal interlocking effects [40–42].

Author Contributions: Conceptualization, E.M. and M.P.; methodology, E.M., M.P., and F.F.; software, E.M.; validation, E.M. and M.P.; formal analysis, E.M., M.P., and F.F.; investigation, M.P.; data curation, M.P.; writing—original draft preparation, M.P.; writing—review and editing, E.M. and F.F.; visualization, E.M., M.P., and F.F.; supervision, E.M. and F.F.; project administration, E.M. All authors have read and agreed to the published version of the manuscript.

Funding: This study is part of the Research Project SUPERCONCRETE (H2020-MSCA-RISE-2014, n. 645704) granted by the EU whose financial support is gratefully acknowledged.

Acknowledgments: The Author wishes to acknowledge the contribution of Agostino De Santis who ran some of the numerical analyses as part of his M.Sc. Thesis in Civil Engineering at the University of Salerno.

Conflicts of Interest: The authors declare no conflict of interest.

References

1. Yoo, D.Y.; Banthia, N. Mechanical properties of ultra-high-performance fiber-reinforced concrete: A review. *Cem. Concr. Compos.* **2016**, *73*, 267–280. [[CrossRef](#)]
2. Grabois, T.M.; Cordeiro, G.C.; Toledo Filho, R.D. Fresh and hardened-state properties of self-compacting lightweight concrete reinforced with steel fibers. *Constr. Build. Mater.* **2016**, *104*, 284–292. [[CrossRef](#)]
3. da Silva, M.A.; Pepe, M.; de Andrade, R.G.M.; Pfeil, M.S.; Toledo Filho, R.D. Rheological and mechanical behavior of high strength steel fiber-river gravel self compacting concrete. *Constr. Build. Mater.* **2017**, *150*, 606–618. [[CrossRef](#)]
4. Torres, J.A.; Lantsoght, E.O. Influence of Fiber Content on Shear Capacity of Steel Fiber-Reinforced Concrete Beams. *Fibers* **2019**, *7*, 102. [[CrossRef](#)]
5. Karimi, M.M.; Darabi, M.K.; Jahanbakhsh, H.; Jahangiri, B.; Rushing, J.F. Effect of steel wool fibers on mechanical and induction heating response of conductive asphalt concrete. *Int. J. Pavement Eng.* **2019**, 1–14. [[CrossRef](#)]
6. Zhu, H.; Zhang, D.; Wang, T.; Wu, H.; Li, V.C. Mechanical and self-healing behavior of low carbon engineered cementitious composites reinforced with PP-fibers. *Constr. Build. Mater.* **2020**, *259*, 119805. [[CrossRef](#)]
7. Ardanuy, M.; Claramunt, J.; Toledo Filho, R.D. Cellulosic fiber reinforced cement-based composites: A review of recent research. *Constr. Build. Mater.* **2015**, *79*, 115–128. [[CrossRef](#)]
8. Ferrara, G.; Pepe, M.; Martinelli, E.; Tolêdo Filho, R.D. Influence of an impregnation treatment on the morphology and mechanical behaviour of flax yarns embedded in hydraulic lime mortar. *Fibers* **2019**, *7*, 30. [[CrossRef](#)]
9. Martinelli, E.; Caggiano, A.; Xargay, H. An experimental study on the post-cracking behaviour of Hybrid Industrial/Recycled Steel Fibre-Reinforced Concrete. *Constr. Build. Mater.* **2015**, *94*, 290–298. [[CrossRef](#)]
10. Spadea, S.; Farina, I.; Carrafiello, A.; Fraternali, F. Recycled nylon fibers as cement mortar reinforcement. *Constr. Build. Mater.* **2015**, *80*, 200–209. [[CrossRef](#)]
11. Frazão, C.M.V.; Barros, J.A.O.; Bogas, J.A. Durability of Recycled Steel Fiber Reinforced Concrete in Chloride Environment. *Fibers* **2019**, *7*, 111. [[CrossRef](#)]
12. Banthia, N.; Sappakittipakorn, M. Toughness enhancement in steel fiber reinforced concrete through fiber hybridization. *Cem. Concr. Res.* **2007**, *37*, 1366–1372. [[CrossRef](#)]
13. Mobasher, B.; Yao, Y.; Soranakom, C. Analytical solutions for flexural design of hybrid steel fiber reinforced concrete beams. *Eng. Struct.* **2015**, *100*, 164–177. [[CrossRef](#)]
14. Farina, I.; Fabbrocino, F.; Carpentieri, G.; Modano, M.; Amendola, A.; Goodall, R.; Fraternali, F. On the reinforcement of cement mortars through 3D printed polymeric and metallic fibers. *Compos. Part B Eng.* **2016**, *90*, 76–85. [[CrossRef](#)]
15. Guerini, V.; Conforti, A.; Plizzari, G.; Kawashima, S. Influence of Steel and Macro-Synthetic Fibers on Concrete Properties. *Fibers* **2018**, *6*, 47. [[CrossRef](#)]
16. Chi, Y.; Yu, M.; Huang, L.; Xu, L. Finite element modeling of steel-polypropylene hybrid fiber reinforced concrete using modified concrete damaged plasticity. *Engineering Structures* **2017**, *148*, 23–35. [[CrossRef](#)]
17. Bošnjak, J.; Sharma, A.; Grauf, K. Mechanical Properties of Concrete with Steel and Polypropylene Fibres at Elevated Temperatures. *Fibers* **2019**, *7*, 9. [[CrossRef](#)]
18. Othman, H.; Marzouk, H.; Sherif, M. Effects of variations in compressive strength and fibre content on dynamic properties of ultra-high performance fibre-reinforced concrete. *Constr. Build. Mater.* **2019**, *195*, 547–556. [[CrossRef](#)]
19. Carvalho, M.R.; Barros, J.A.; Zhang, Y.; Dias-da-Costa, D. A computational model for simulation of steel fibre reinforced concrete with explicit fibres and cracks. *Comput. Methods Appl. Mech. Eng.* **2020**, *363*, 112879. [[CrossRef](#)]
20. Farina, I.; Modano, M.; Zuccaro, G.; Goodall, R.; Colangelo, F. Improving flexural strength and toughness of geopolymer mortars through additively manufactured metallic rebars. *Compos. Part B Eng.* **2018**, *145*, 155–161. [[CrossRef](#)]
21. Abed, F.; Alhafiz, A.R. Effect of basalt fibers on the flexural behavior of concrete beams reinforced with BFRP bars. *Compos. Struct.* **2019**, *215*, 23–34. [[CrossRef](#)]
22. ASTM C1018-97. *Standard Test Method for Flexural Toughness and First-Crack Strength of Fiber-Reinforced Concrete (Using Beam with Third-Point Loading)*; ASTM International: West Conshohocken, PA, USA, 1997.

23. RILEM-TC-162-TDF. Test and design methods for steel fibre reinforced concrete—bending test, final recommendation. *Mater. Struct.* **2002**, *35*, 579–582. [[CrossRef](#)]
24. EN 14651. *Test Method for Metallic Fibred Concrete—Measuring the Flexural Tensile Strength (Limit of Proportionality (LOP), Residual)*; CEN: Brussels, Belgium, 2005.
25. UNI 11039-1. *Steel Fiber Reinforced Concrete—Definitions, Classification and Designation*; UNI: Milan, Italy, 2003.
26. UNI 11039-2. *Steel Fiber Reinforced Concrete—Test Method to Determine the First Crack Strength and Ductility Indexes*; UNI: Milan, Italy, 2003.
27. Code, M. *Fib Model Code for Concrete Structures 2010*. *Fédération Internationale du Béton*; Ernst & Sohn: Berlin, Germany, 2013; p. 434.
28. Hu, X.D.; Day, R.; Dux, P. Biaxial failure model for fiber reinforced concrete. *J. Mater. Civ. Eng.* **2003**, *15*, 609–615. [[CrossRef](#)]
29. Li, F.; Li, Z. Continuum damage mechanics based modeling of fiber reinforced concrete in tension. *Int. J. Solids Struct.* **2001**, *38*, 777–793. [[CrossRef](#)]
30. Beghini, A.; Bažant, Z.P.; Zhou, Y.; Gouirand, O.; Caner, F.C. Microplane model M5f for multiaxial behavior and fracture of fiber-reinforced concrete. *J. Eng. Mech.* **2007**, *133*, 66–75. [[CrossRef](#)]
31. Ramm, E.; Hund, A.; Hettich, T. A variational multiscale model for composites with special emphasis on the X-FEM and level sets. In *Computational Modelling of Concrete Structures: Proceedings of the EURO-C*; CRC Press: Boca Raton, FL, USA, 2006; pp. 27–30.
32. Caggiano, A.; Etse, G.; Martinelli, E. Zero-thickness interface model formulation for failure behavior of fiber-reinforced cementitious composites. *Comput. Struct.* **2012**, *98*, 23–32. [[CrossRef](#)]
33. El-Helou, R.G.; Moen, C.D.; Lale, E.; Cusatis, G. Lattice discrete particle modeling of buckling deformation in thin ultra-high-performance fiber-reinforced concrete plates. *Comput. Model. Concr. Struct.* **2014**, *1*, 365–371. [[CrossRef](#)]
34. Hillerborg, A.; Modeer, M.; Petersson, P.E. Analysis of Crack Formation and Crack Growth in Concrete by Means of Fracture Mechanics and Finite Elements. *Cem. Concr. Res.* **1976**, *6*, 773–781. [[CrossRef](#)]
35. Olesen, J.F. Fictitious crack propagation in fiber-reinforced concrete beams. *J. Eng. Mech.* **2001**, *127*, 272–280. [[CrossRef](#)]
36. Armelin, H.S.; Banthia, N. Predicting the flexural postcracking performance of steel fiber reinforced concrete from the pullout of single fibers. *Mater. J.* **1997**, *94*, 18–31.
37. Caggiano, A.; Folino, P.; Lima, C.; Martinelli, E.; Pepe, M. *On the mechanical response of hybrid fiber reinforced concrete with recycled and industrial steel fibers*. *Constr. Build. Mater.* **2017**, *147*, 286–295. [[CrossRef](#)]
38. Caggiano, A.; Gambarelli, S.; Martinelli, E.; Nisticò, N.; Pepe, M. Experimental characterization of the post-cracking response in hybrid steel/polypropylene fiber-reinforced concrete. *Constr. Build. Mater.* **2016**, *125*, 1035–1043. [[CrossRef](#)]
39. Farina, I.; Goodall, R.; Hernández-Nava, E.; di Filippo, A.; Colangelo, F.; Fraternali, F. Design, microstructure and mechanical characterization of Ti6Al4V reinforcing elements for cement composites with fractal architecture. *Mater. Des.* **2019**, *172*, 107758. [[CrossRef](#)]
40. Khoshhesab, M.M.; Li, Y. Mechanical behavior of 3D printed biomimetic koch fractal contact and interlocking. *Extreme Mech. Lett.* **2018**, *24*, 58–65. [[CrossRef](#)]
41. Li, Y.; Ortiz, C.; Boyce, M.C. A generalized mechanical model for suture inter-faces of arbitrary geometry. *J. Mech. Phys. Solids* **2013**, *61*, 1144–1167. [[CrossRef](#)]
42. Farina, I.; Fabbrocino, F.; Colangelo, F.; Feo, L.; Fraternali, F. Surface roughness effects on the reinforcement of cement mortars through 3D printed metallic fibers. *Compos. Part B Eng.* **2016**, *99*, 305–311. [[CrossRef](#)]

